

Enhanced Mixing at Inertial Microscales using Flow-Induced Flutter

Aaron Rips¹ and Rajat Mittal¹

¹ Mechanical Engineering, Johns Hopkins University, Baltimore, Maryland

Abstract

Numerical simulations are used to explore the use of flow-induced flutter of a membrane as a mechanism for effective mixing at inertial microscales. A simple two-dimensional model of mixing in a channel is employed and fluid-structure interaction modeling with an immersed boundary method-based solver is used to explore the flow physics, flutter dynamics and scalar mixing of these flutter mixers. The performance of the mixers is characterized in terms of a mixing index and a non-dimensional head loss, and the effect of Reynolds and Schmidt numbers, as well as the membrane length on these performance indices, is examined. Simulations indicate that flow-induced flutter is capable of significantly enhancing mixing for channel Reynolds numbers as low as 15 and the relatively low associated pressure loss might make these flutter mixers a viable alternative for such applications.

Introduction

Mixing enhancement at the so-called inertial scale Reynolds numbers i.e. $O(1) < Re < O(100)$ (1) has wide ranging applications in both chemical and biomedical engineering. Recent interest in this arena has been driven by the development of lab-on-a-chip (LOC) devices, micro-total-analysis systems (μ TAS) and other low cost, field deployable, chemical or biological microfluidic devices (2-8). These microfluidic devices involving either analysis or synthesis in biological or chemical applications, often require fast mixing. However, high throughput assays require increased operational flow rates, which increases Reynolds and Peclet numbers, thereby reducing transverse molecular transport. On the other hand, the Reynolds number of these flows remain too low to take advantage of mixing due to turbulence or other intrinsic fluid-dynamic instabilities (e.g. vortex shedding). The challenge then is to create devices which can accomplish efficient mixing without relying on these mechanisms. Within this context, inertial micromixers may be categorized as “active” or “passive.” Active mixing involves addition of energy beyond the pumping power required to move the fluid, and may be in the form of pressure perturbations (9-11), or mechanical (12, 13), electromagnetic (14, 15), acoustic (16, 17), or piezoelectric energy (18), as well as many other approaches. Active mixers introduce spatial and temporal variations into the flow which enhance mixing. This approach can be very effective, but it adds significant complexity, which increases cost and decreases system reliability.

Passive mixers require no external forcing, but instead, use only the energy of flow (i.e. pumping power) to induce mixing. The use of complex channel paths (curved, sinusoids, zig-zags, and square wave shapes etc.) is a common passive mixing technique (6, 19, 20). Other devices such as the so-called chaotic advection mixers use obstacles to introduce complex, spatially varying velocity gradients into the flow as a way to enhance mixing (21). While these passive mixers have a simpler design, they usually underperform compared to active mixers (3, 22). This is because these passive mixers are always “static” and do not introduce any temporal fluctuations into the flow. Furthermore, these passive mixers also

incur large pressure losses and this manifests as increased pumping power as well as higher channel pressures, both of which are undesirable in microfluidic systems (3).

In the current paper, we explore a new approach to inertial micromixing; one that exploits flow-induced flutter of membranes to enhance mixing. These “flutter mixers” may be considered passive in that they do not require any energy input beyond the pumping power that drives the flow. However, their effect is akin to active mixers in that they introduce complex spatial as well as temporal fluctuations into the flow. These flutter micromixers have several desirable traits: first, the flutter instability occurs over a wide range of Reynolds numbers relevant to inertial micromixing and their mixing performance improves with increasing Reynolds number; second, the structural parameters (density and elasticity) of the fluttering element can in-principle be chosen to optimize the flutter for a given mixing application; third, the device complexity should be lower than active mixers; and finally, as will be shown, significant mixing enhancement can be accomplished with a relatively small attendant pressure loss.

Our previous study examined the use of membrane flutter in channels to enhance heat transfer in heat-sinks appropriate for electronic cooling applications (23-25). The Reynolds numbers for these applications is typically $O(1000)$ or higher (23) where membrane flutter is guaranteed, although the simulations did show sustained flutter at a Reynolds number of 50. Past experimental work on flapping flags/membranes/filaments has also been at $O(1000)$ or higher Reynolds numbers (see (26-33)) while a significant number of computational modeling studies have employed inviscid models (34-42). Even modeling studies employing viscous flow models have mostly focused on Reynolds number of $O(100)$ or higher (43-45). Thus, much of the previous work is not directly relevant to the inertial micromixing regime where Reynolds numbers extend down to $O(10)$ and viscous effects are much more significant.

The current paper focuses on flow-induced membrane flutter in the $O(10-100)$ Reynolds number regime that is relevant for inertial micromixing, and provides a detailed description of the flutter dynamics, flow features and mixing. We employ flow simulations in a simple two-dimensional (2D) model of an inertial scale micromixer and examine the effect of key parameters such as Reynolds and Schmidt numbers, as well as reduced velocity and confinement ratio on the flutter dynamics, flow/vortex features, pressure losses and mixing quality. We also explore strategies for extending downwards, the range of Reynolds number for which such mixers could be used.

Computational Model

Configuration and Governing Equations

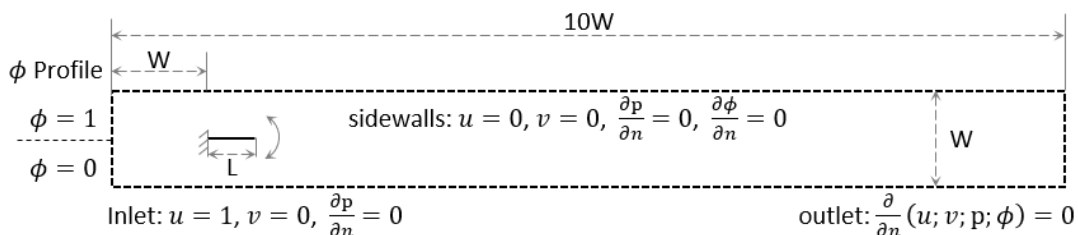


FIG. 1 – Schematic diagram of the computational domain (not to scale) showing the geometry and boundary conditions.

As shown in FIG. 1 in this study, we investigate the mixing enhancement associated with flow-induced flutter of a flexible membrane in a 2D channel of width W , length $10W$ and with a mean flow velocity U .

Physical Review Fluids, 4(5), p.054501

<https://doi.org/10.1103/PhysRevFluids.4.054501>

The membrane has length L and is placed on the center-line of the channel a distance W downstream of the entrance. This fluid-structure-scalar multiphysics system exhibits two-way coupling between the fluid and structure and one way coupling between the fluid and the scalar. The typical channel widths at which such flutter mixers could be fabricated and operated ranges from $O(100)$ to $O(1000)$ microns and the continuum approximation and no-slip conditions are acceptable at these scales (46). The flow is assumed to be governed by the incompressible Navier-Stokes equations. The membrane, which is assumed to be inextensible, is governed by the Navier equations expressed in terms of the position vector \mathbf{X} and the tension ζ of the membrane; and the scalar ϕ is governed by an advection-diffusion equation. The system's governing equations in the non-dimensional form are as follows:

$$\frac{\partial \mathbf{u}}{\partial t} + \nabla \cdot (\mathbf{u}\mathbf{u}) = -\nabla p + \frac{1}{\text{Re}} \nabla^2 \mathbf{u} + \mathbf{f} \quad (1)$$

$$\nabla \cdot \mathbf{u} = 0 \quad (2)$$

$$\frac{\partial \phi}{\partial t} + \mathbf{u} \cdot \nabla \phi = \frac{1}{\text{Re} \cdot \text{Sc}} \nabla^2 \phi \quad (3)$$

$$\frac{\partial^2 \mathbf{X}}{\partial t^2} = \frac{\partial}{\partial s} \left(\zeta \frac{\partial \mathbf{X}}{\partial s} \right) - \frac{\partial^2}{\partial s^2} \left(\frac{M^*}{U^{*2}} \frac{\partial \mathbf{X}}{\partial s} \right) - M^* \mathbf{F} \quad (4)$$

$$\frac{\partial \mathbf{X}}{\partial s} \cdot \frac{\partial^2}{\partial s^2} \left(\zeta \frac{\partial \mathbf{X}}{\partial s} \right) = \frac{1}{2} \frac{\partial^2}{\partial t^2} \left(\frac{\partial \mathbf{X}}{\partial s} \cdot \frac{\partial \mathbf{X}}{\partial s} \right) - \frac{\partial^2 \mathbf{X}}{\partial t \partial s} \cdot \frac{\partial^2 \mathbf{X}}{\partial t \partial s} - \frac{\partial \mathbf{X}}{\partial s} \cdot \frac{\partial}{\partial s} (\mathbf{F}) \quad (5)$$

For the fluid governing equations (1) and (2), \mathbf{u} is the velocity field, t is time, p is pressure, Re is the Reynolds number defined as $\text{Re} = UW / \nu$ where U is the mean inlet velocity, W is the characteristic length given by the width of the channel, and ν is the dynamic viscosity of the fluid. Furthermore, \mathbf{f} is a forcing function associated with the fluid-structure interaction penalty method which will be discussed in a following section. For the scalar equation (3), ϕ is the scalar concentration ranging from 0 to 1, and Sc is the Schmidt number defined as $\text{Sc} = \nu/D$ where D is the mass diffusivity of the scalar. Equations (4) and (5) govern the position and tension of the membrane. The key non-dimensional parameters governing the structure are the mass ratio M^* and reduced velocity U^* :

$$M^* = \frac{\rho L}{m_s}, \quad U^* = UL \sqrt{\frac{m_s}{k_b}} \quad (6)$$

In the above, k_b is the bending rigidity. m_s is the excess mass per unit length according to $m_s = m_m - \rho_f A_s$ where m_m is the mass per unit length of the membrane, ρ_f is the density of the fluid, and A_s is the cross-sectional area of the membrane. For the cases studied here, $A_s \rightarrow 0$ (the limit of a thin element), so $m_s \sim m_m$. \mathbf{F} is the force density induced by the element on the surrounding fluid associated with the fluid-structure interaction penalty forcing method. Equation (5) is a Poisson's equation for the tension derived as described in Huang et. al. (43) by applying an inextensibility constraint defined as $(\partial \mathbf{X} / \partial s) \cdot (\partial \mathbf{X} / \partial s) = 1$ to equation (4).

Parameters and Boundary Conditions

In this study the range of Reynolds numbers based on the channel width W is 10 to 200 and Sc was varied in large increments from 1 to 1000. Three membrane lengths were studied: $L=W/2$, $L=W$, and $L=2W$. Based

Physical Review Fluids, 4(5), p.054501

<https://doi.org/10.1103/PhysRevFluids.4.054501>

on prior work on confined flapping membranes (24) M^* and U^* were chosen as 0.5 and 15 respectively for the initial set of simulations so as to generate large amplitude flutter at these Re numbers. Later sections of paper explore flags with different lengths as a way to modulate U^* . The final range of the non-dimensional parameters in the current study is as follows:

$$\text{Re: } 10\text{-}200; M^*: 0.25 - 1.0; U^*: 7.5 - 30; L/W: 0.5 - 2.0; Sc: 1 - 1000.$$

The developing flow in the channel has a uniform inlet boundary condition $u(0,y,t)=1$, Dirichlet no-slip boundary conditions on the sidewalls, Neumann boundary conditions at the outflow, and an initial value of $u(x,y,0)=1$ everywhere. The leading-edge of the membrane is fixed and the trailing edge is free, with the corresponding boundary conditions being:

$$\mathbf{x} = \mathbf{x}_0, \quad \frac{\partial \mathbf{x}}{\partial s} = [1, 0] \quad \text{at } s=0 \text{ (leading-edge: fixed)} \quad (7)$$

$$M = \gamma = 0 \quad \text{at } s=L \text{ (trailing edge: free)} \quad (8)$$

where M is the bending moment along the membrane. The membrane is initially deflected slightly (by a 2.5° angle to the incoming flow) to accelerate the attainment of stationary state. Verification studies have been performed to ensure that the dynamics are not sensitive to this small initial perturbation. The inlet boundary condition for the velocity is $U=1$ and the initial condition for the scalar field ϕ is as follows:

$$\begin{aligned} \phi &= 0 & 0 < y < W/2 & \text{ (bottom half of channel)} \\ \phi &= 1 & W/2 < y < W & \text{ (top half of channel)} \end{aligned} \quad (9)$$

Numerical Method

The governing equations were solved using the in-house code ViCar3D which uses a second-order fractional step method on collocated Cartesian grids (47). The 2nd-order Crank-Nicolson fully implicit scheme is used for convective and diffusion terms and the Pressure Poisson equation is then solved with the biconjugate gradient (BiCGSTAB) scheme (48). Further details of the method can be found in Mittal et. al. (47) and Seo et. al. (49) and validation and benchmarking for flow-induced flutter problems can be found in Shoele & Mittal (24, 50).

Given that the immersed boundary method used in this study has been described in previous publications (24, 50, 51), only a brief summary of the method is included here. The membrane's velocity $\mathbf{U}(s,t)$ and coupling force density $\mathbf{F}(s,t)$ are translated to the fluid's velocity $\mathbf{u}(\mathbf{x},t)$ and coupling force density $\mathbf{f}(\mathbf{x},t)$ using delta functions according to:

$$\mathbf{U}(s,t) = \int_{\Omega_f} \mathbf{u}(\mathbf{x},t) \delta[\mathbf{x} - \mathbf{X}(s,t)] d\mathbf{x} \quad (10)$$

$$\mathbf{f}(\mathbf{x},t) = \int_{\Gamma} \mathbf{F}(s,t) \delta[\mathbf{x} - \mathbf{X}(s,t)] ds \quad (11)$$

where Ω_f is the fluid domain, Γ is the surface of the membrane, and δ is the Dirac-delta function. To create this coupling force, a penalty method is used (52). The fluid and structure solutions are first calculated independently; following this the new penalty momentum force is calculated using two sets of

Physical Review Fluids, 4(5), p.054501

<https://doi.org/10.1103/PhysRevFluids.4.054501>

points along the membrane. The first set of points are the structure's Lagrangian grid points and the second set are massless virtual points which follow the local fluid velocity. The penalty momentum force $\mathbf{F}(s,t)$ can then be characterized as a spring-damper system that "connects" the two sets of structure points according to the following equation:

$$\mathbf{F}(s,t) = -K_p \frac{\rho U^2}{L} [(\tilde{\mathbf{X}} - \mathbf{x}) + \beta \Delta t (\tilde{\mathbf{U}} - \mathbf{U})] \quad (12)$$

where K_p is a large penalty constant, β is penalty constant, and Δt is the computational time step. Based on a prior sensitivity analysis (51), these parameters were chosen as $K_p = -10^5$, $\beta = 150$, and $dt = 1.0 \times 10^{-4}$. The massless fluid following points' positions and velocities are $\tilde{\mathbf{X}}$ and $\tilde{\mathbf{U}}$ which are computed from the current and previous fluid velocities as:

$$\frac{d\tilde{\mathbf{X}}}{dt} = \tilde{\mathbf{U}}(s,t); \quad \tilde{\mathbf{U}}(s,t) = \int_{\Omega_f} \mathbf{u}(\mathbf{x},t) \delta[\mathbf{x} - \tilde{\mathbf{X}}(s,t)] d\mathbf{x} \quad (13)$$

The fluid-structure-scalar equations are discretized and solved following prior work in (24, 51). The fluid and scalar equations are solved on uniform Cartesian grids in a $10W$ by W domain with $dx=dy=0.008W$ resulting in 1280×128 grid points. Uniform grids were chosen to resolve the large gradients in the scalar field at high Schmidt numbers. The membrane grid employs 80 points which provides high resolution for the structural dynamics. Results from the grid convergence study are provided in the Appendix. The simulations were run for roughly 10 flow-through times ($O(10^6)$ time steps) and statistics accumulated over the last four flow-through times.

Data Analysis and Performance Metrics

To systematically evaluate the performance of these membranes, the mixing effectiveness as well as the loss of mechanical energy must be quantified. Mixing has been quantified by a variety of metrics in the past (53-55) and here we use the so-called mixing index (M) which is defined at a given streamwise location as:

$$M(x) = 1 - \sqrt{\frac{\sigma(x)^2}{\sigma_{\max}^2}} \quad \text{where} \quad \sigma(x) = \sqrt{\frac{1}{W} \int_0^W (\phi(x,y) - \bar{\phi}_m(x))^2 dy} \quad (1)$$

is the standard deviation, ϕ is the scalar field ranging from 0 to 1, $\bar{\phi}_m$ is the mean of the field and σ_{\max} is the maximum deviation in the scalar field, which occurs at the inlet. Thus the mixing index M is just the normalized variance of the scalar concentration and it ranges from 0 to 1 with $M=0$ indicating totally unmixed flow and $M=1$, complete mixing.

The loss in mechanical energy is estimated by computing the non-dimensional head (H) and corresponding head loss (HL) through the channel:

$$H^*(x) = \frac{H(x)}{\rho U^2} = \int_0^H \left(\rho(x,y) + \frac{1}{2} u^2(x,y) \right) dy; \quad HL^*(x) = H^*(0) - H^*(x) \quad (2)$$

Results

The results are organized as follows: we first present the effect of Reynolds number on the performance of the flutter mixer; this is followed by an examination of the effect of membrane length and mass diffusivity on the mixing performance. Finally, we compare the performance of the flutter mixer to a conventional “post” mixer and provide an overview of the performance comparisons for all the cases.

Effect of Reynolds Number

The goal of this study is to investigate the mixing performance of these flutter mixers at inertial-microscale Reynolds numbers and we initially examined the flutter characteristics for a membrane with length $L=W/2$ over the Reynolds number range from 25-200 which is relevant for inertial-scale micromixing applications.

The Schmidt number for this study is fixed at 100, which lies squarely within the range of Schmidt numbers relevant for these applications (3). FIG. 2 show the motion envelopes of the membrane as well as the trailing-edge amplitude and Strouhal number as a function of the Reynolds number. The plot shows that the amplitude is nearly zero at $Re=25$; low amplitude flutter is seen at $Re=37.5$ and substantial flutter is observed for $Re=50$ and beyond. The flutter amplitude exhibits an asymptotic behavior with Reynolds number, with the amplitude only growing from about $y_{max}/W=0.285$ to 0.33 between $Re=100$ and 200, indicating a saturation of the flutter behavior of this configuration with increasing Re number. The frequency of flutter (f_m) as characterized by the Strouhal number ($St_w = f_m W/U$) is nearly constant at a value of about 0.66 for cases with substantial flutter amplitude.

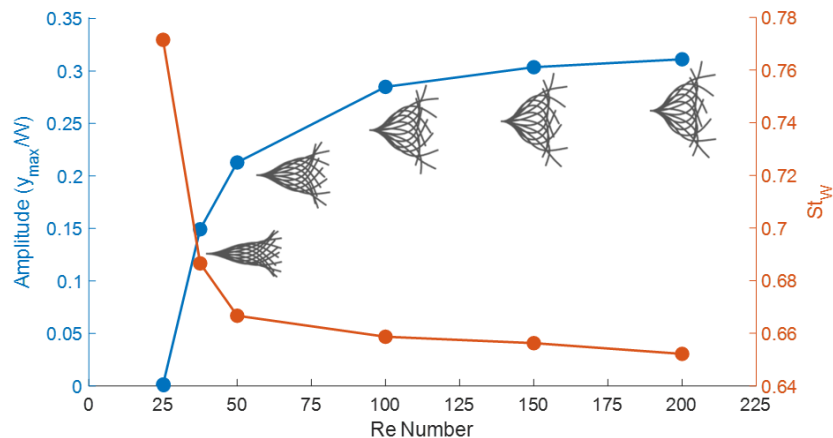


FIG. 2 – Flapping amplitude and Strouhal Number vs. Re number, measured from the maximum y component of the tip position.

FIG. 3 shows contours of spanwise vorticity for four selected cases and these show that for Reynolds numbers beyond 100, the essential features of the vortex topology include the rolling up of the shear layers on the membrane and shedding of compact vortices into the wake. These vortices arrange themselves in an inverse Karman vortex street, wherein the counter-clockwise rotating vortices are above the clockwise rotating vortices. Such vortex streets are typically seen in thrust generating flapping foils (56). The literature on flapping membranes/flags seems to indicate that confinement changes the resulting vortex street from a standard Karman street to an inverse Karman street. This is discussed directly in Alben (36) where they show a reverse Karman vortex street for confined flags using an analytical vortex sheet method over a range of confinement ratios. Similarly, the previous work of Shoele & Mittal (24) found inverse vortex streets over a wide range of flutter amplitudes for $Re=400$ for a range of confinement ratios. In contrast, other papers (43-45) examining unconfined flapping membranes showed

that, at least for the periodic flapping regime, the membrane creates a standard Karman vortex street. For the Reynolds number of 50, the vortex rollup is not clearly visible, although individual counter-rotating vorticity is still shed in the wake at each half of the flapping cycle. These vortices seem to dissipate rapidly in the near wake. For the lowest Reynolds number of 25, there is no vortex shedding in the wake of the membrane, which is observed to remain stationary.

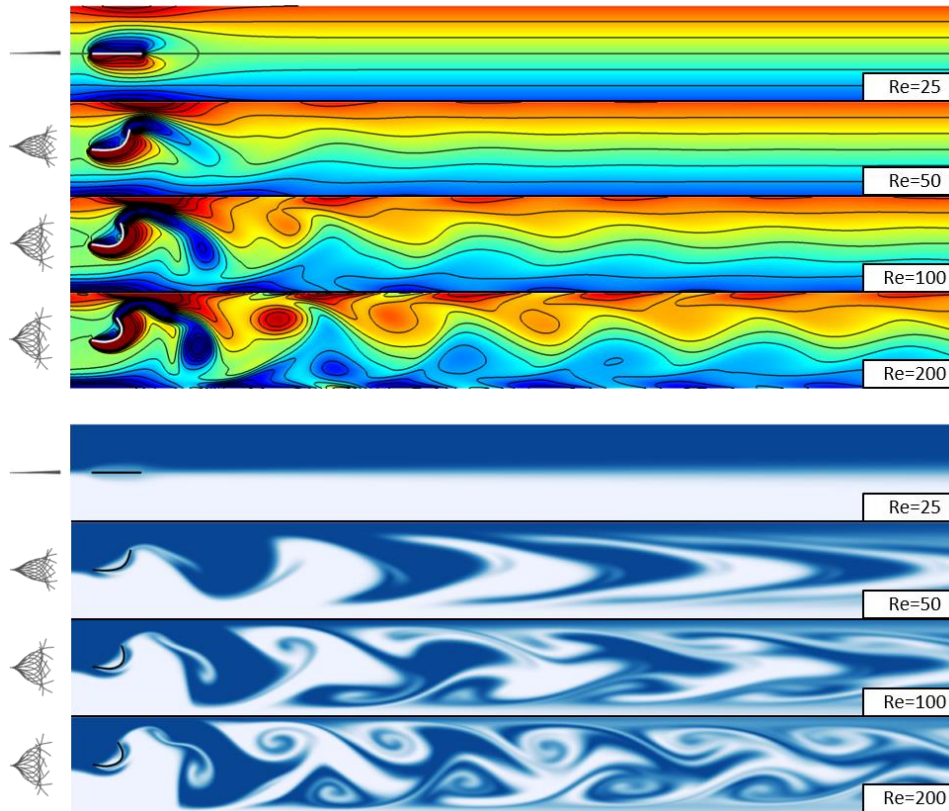


FIG. 3 – Contour plots of spanwise vorticity (top) and scalar concentration (bottom) for $L=W/2$ membrane at Reynolds numbers of 25, 50, 100, 200. The images to the left of the contour plots show the motion envelopes for the membrane through one cycle.

The characteristics of the scalar field (shown in FIG. 3) reflect the underlying vortex topology. For the $Re=50$ case, the vortex shedding is quite weak and the primary perturbation to the scalar field comes directly from the movement of the membrane. This movement generates nearly sinusoidal deformation of the scalar interface in the near wake of the membrane and as this deformed interface advects downstream, it is stretched along the streamwise direction due to the strain-rate associated with the parabolic flow profile. This stretching is beneficial for mixing since it increases the interface length and sharpens the scalar gradients, thereby facilitating diffusive mixing.

For Reynolds number of 100 and higher, two factors significantly accelerate the mixing process. First, with a larger flapping amplitude, the perturbations in the scalar field generated directly by the membrane motion are larger. Furthermore, and more importantly, the compact vortices shed at the end of each half-stroke entrain scalar from one side of the channel and advect it to the other side. It is also observed that in addition to the continuous downstream stretching of the interface due to the parabolic velocity field, the shed vortices continue to entrain mass thereby further enhancing the deformation of the scalar interface. This of course, further accelerates the process of diffusive mixing. Thus, the flutter mixers are

expected to continue to perform well beyond Reynolds numbers of 200 although intrinsic three-dimensional effects, likely become important at these higher Reynolds numbers.

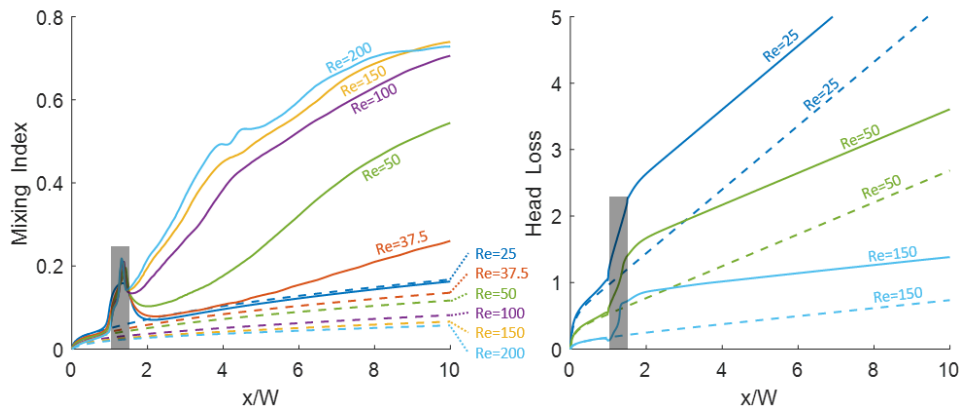


FIG. 4 – Plots of time averaged mixing index (left) and head loss (right) as a function of downstream location. The solid lines are the flapping membrane cases and the dashed lines are the empty channel baseline cases for comparison. Only three selected cases are shown in the head loss plot. The shaded vertical bands represent the region occupied by the membrane.

Considering the plot for head loss, it is clear that the flapping membrane accounts for a noticeable increase in head loss. However, it will be shown later that these losses are significantly smaller than those associated with another typical mixing enhancement method (57) which is discussed in a later section. This increased head loss is in principle associated with the viscous drag on the membrane, as well as the energy associated with the flapping of the membrane, and the vortex structures created by the membrane. However, it is also noted that the head loss for the flutter mixer rapidly establishes a linear increase downstream of the membrane with a slope that matches that of the empty channel case. This implies that the kinetic energy (or dynamic pressure) term contributes very little to the increase in head loss, and almost all the head loss is associated with an increase in the static pressure. Interestingly, the increase in the static pressure is still significant for the $Re=25$ case which did not exhibit flutter, suggesting that the viscous drag on the membrane is the dominant factor contributing to the additional pressure loss.

Effect of Membrane Length and Minimum Effective Reynolds Number

The lack of flutter at $Re=25$ for the $L=W/2$ case is not entirely surprising since it is known that viscous effects tend to damp the fluid-elastic instability (58) and increase the critical reduced velocity at which flutter occurs. From the viewpoint of establishing the operational range of these mixers, it is useful to determine the lower limit of Reynolds numbers for which these micromixers can work. The reduced velocity can be rewritten as $U^* = U(L/t)\sqrt{\rho_s/E}$ where t is the thickness of the membrane and E it's Young's modulus. This suggests that the reduced velocity for a membrane could be increased for a given Reynolds number by either increasing the length or reducing the thickness of the membrane. The same could be accomplished by reducing the elastic modulus or increasing the density of the membrane material. Here we explore the simple and more easily realizable strategy of increasing the membrane length and have simulated two additional cases with $L=W$ and $2W$ at the low Reynolds numbers ($Re \leq 25$). It should be noted that increasing the membrane length also increases the confinement (i.e. L/W). Since increase in confinement is known to reduce the critical U^* for flutter (36), this should further promote the flutter tendency of the confined membrane.

FIG. 5 includes the flutter amplitude for these cases and we note that minimum non-zero flutter amplitudes are $y_{\max}/W=0.14$ at $Re=20$ for the $L=W$ case and $y_{\max}/W=0.28$ at $Re=15$ for the $L=2W$. Thus, the longest membrane flutters with a significantly larger amplitude at $Re=20$ than the $L=W/2$ case reached even at $Re=200$.

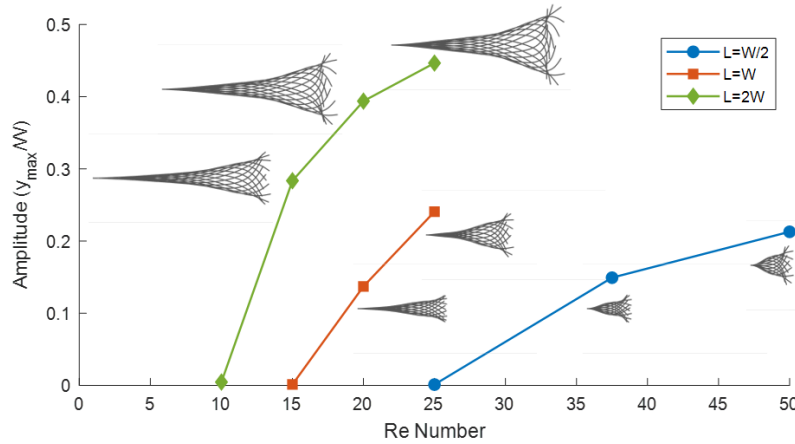


FIG. 5 – Flutter amplitude (y_{\max}/W) and envelopes for the $L=W/2$, W , and $2W$ cases for low Reynolds numbers.

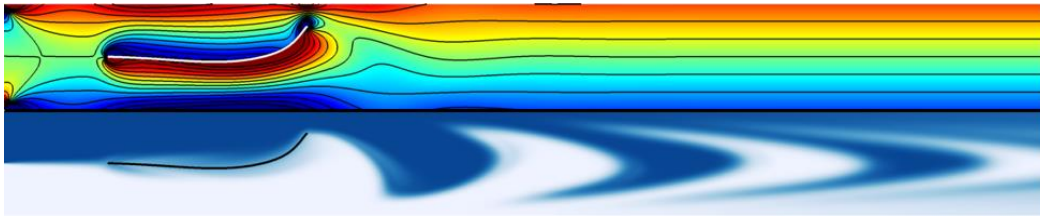


FIG. 6 – Spanwise vorticity (ω_z) and scalar concentration (ϕ) for the $L=2W$, $Re=15$ case.

FIG. 6 shows the spanwise vorticity and scalar field for the $L=2W$ $Re=15$ case, which is the lowest Re number where flutter was observed in this study. It is noted that the overall features are quite similar to those for the $L=W/2$ membrane at $Re=50$ wherein no compact vortices are shed, and the only mixing enhancement is due to the initial sinusoidal deformation of the scalar interface and the subsequent stretching by the parabolic flow profile.

FIG. 7 summarizes the overall performance of the various cases examined in the current study at $Sc=100$. In this figure we plot the mixing index at the exit of the mixer ($x/W=10$) against the total non-dimensional pressure loss. The plot clarifies the trends in the mixer performance of this system for various Reynolds numbers and membrane lengths. For the empty channel, mixing occurs exclusively due to molecular diffusion and the mixing index increases slowly with decreasing Reynolds number (at fixed Schmidt number). Even at the lowest Reynolds number, the mixing index only reaches about 0.3 at the end of the channel. In contrast, for the channel with the flag ($L=W/2$), the mixing index rises rapidly with Reynolds number and reaches a peak of 0.78 at $Re=150$. This confirms that advective effects dominate the mixing process in the flutter mixer. The flutter mixer with $L=W$ has a mixing index at $Re=25$ that is nearly the same as that for $L=W/2$ and $Re=50$, although the pressure loss is nearly twice the value. Also, the $Re=20$ case for this membrane sees only marginally better mixing than the corresponding empty channel, while incurring a 30% larger head loss. Finally, the $L=2W$ case exhibits significant flutter and associate mixing

enhancement down to a Reynolds number of 15 although, the associated pressure losses are quite significant.

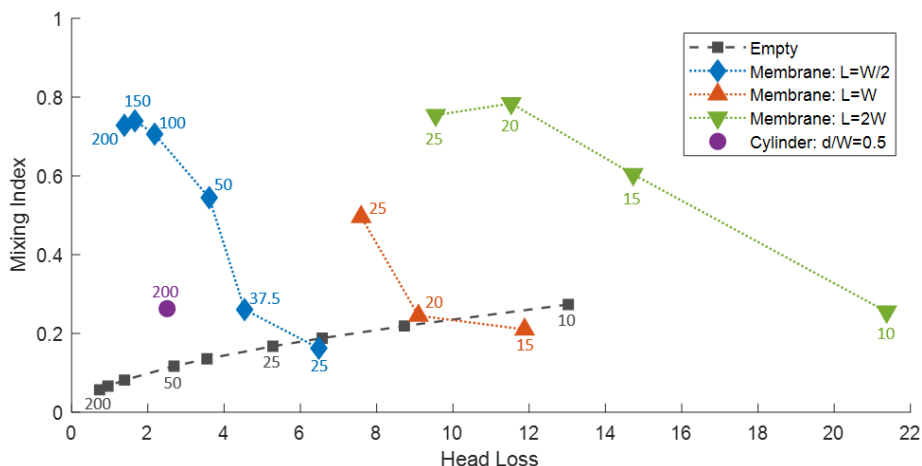


FIG. 7 – Performance comparison in terms of pressure drop and mixing index for the various cases studied in this paper. The Reynolds number for each case is noted on the plot. The point corresponding to the cylinder is discussed in a later section.

Given the increase in pressure drop associated with increasing membrane length, other strategies such as reducing the thickness or changing the material properties of the membrane could, in principle be explored. All of these strategies would likely not increase the pressure drop significantly, but might be challenging from a materials selection and/or fabrication viewpoint. Exploration of these strategies is outside the scope of the current study.

Effect of Schmidt Number

Mass diffusivities may vary over a large range in micromixing applications (3) and it is therefore useful to examine the effect of variations in this property on the performance of the flutter mixers. For this study, we fix the Reynolds number to 200 and vary the Schmidt number (Sc) from 1 to 1000. FIG. 8 shows snapshots of the scalar field at $Sc = 1, 10, 100,$ and 1000 (3). The observed behavior of the scalar is as expected: the flapping and vortex shedding only depends on the Reynolds number and is therefore the same for all these cases. However, the higher relative mass diffusivities at the lower Schmidt numbers ($Sc=1,10$) leads to stronger diffusive mixing across the scalar interfaces produced by vortex shedding and convection of the shed vortices. The $Sc=100$ and 1000 cases exhibit nearly identical scalar patterns indicating that beyond about $Sc=100$, the mixing is dominated by advection, at least within the channel length examine here.

The plot of the time-averaged mixing index in FIG. 9 provides a more quantitative measure of the effect of Schmidt number. Since the head loss depends only on the Reynolds number, its variation remains the same as that shown in FIG. 4. For the empty channel, the mixing performance increases significantly with reduction in Schmidt number due to the increase in mass diffusivity. For the flutter mixer with $Sc=1.0$, the scalars are almost fully mixed ($M=0.99$) by $x/W=10$, whereas for the highest Schmidt number of 1000, $M=0.65$ at $x/W=10$, which significantly exceeds the corresponding value for the empty channel ($M=0.02$). Overall, for the $Sc = 1, 10, 100,$ and 1000 cases, the flutter mixer improves the mixing index by factors of 1.4, 4.1, 11.7, and 37.1, respectively, over their respective baselines. Thus, the introduction of the membrane significantly enhances the mixing performance for every case explored here.

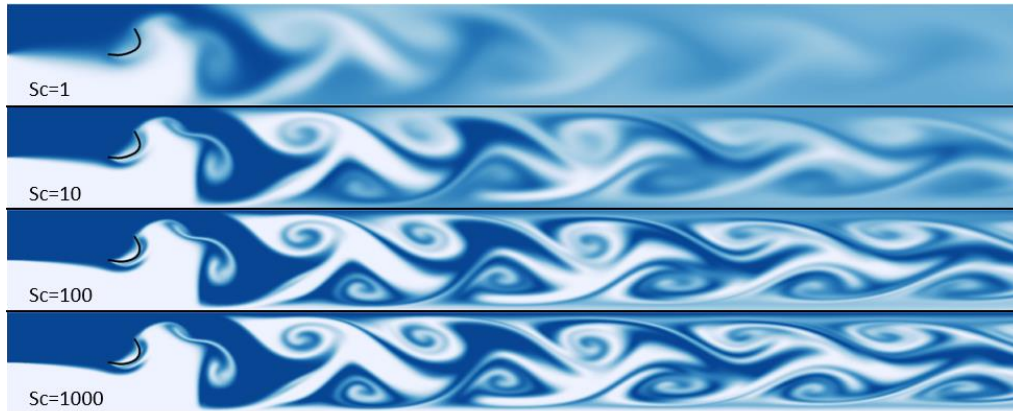


FIG. 8 – Contour plots show instantaneous snapshots of the scalar concentration field ϕ for $Sc = 1, 10, 100, 1000$.

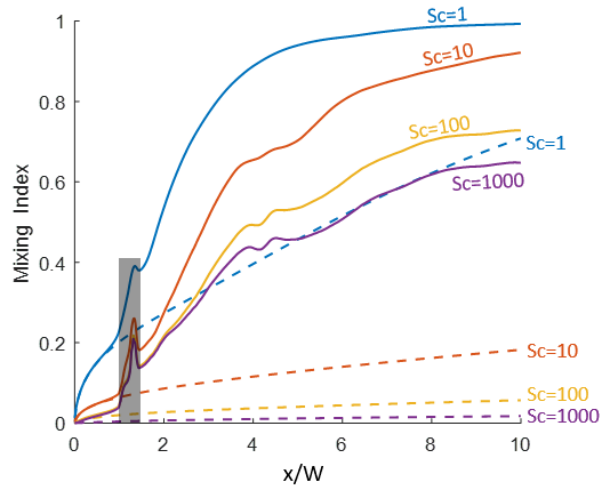


FIG. 9 – Plots of time averaged mixing index vs. downstream location for $Re=200$ and $Sc = 1, 10, 100, 1000$. Shaded areas depict the extent of the membrane.

Comparison with Bluff-Body Induced Mixing

To better understand the performance of the flutter mixer, it is useful to compare it with other passive mixers. However, since there are so many different passive mixer designs (3, 5, 6, 8), it is difficult to establish a systematic approach to this comparison. In the current study, we choose to compare the flutter mixer to a mixer that employs a bluff-body to induce vortex shedding and mixing. Such mixers (sometimes called “post” micromixers) have been proposed before (57) and the advantage of comparing with these mixers is that both use vortex formation and shedding as the primary mechanism for enhanced mixing.

The cylinder in the channel introduces the additional parameter (d/W), where d is the cylinder diameter. In the current study, we have simulated flow for $d/W = 0.25, 0.50$ and 0.75 for $Re=200$ and $Sc=100$. No vortex shedding is observed for the smallest and largest cylinders at this Re number. For the smallest cylinder, the diameter-based Reynolds number $Re_d = (dU/\nu)$ is 50 and this is close to the critical Reynolds number for vortex shedding. For the largest cylinder, the flow and the vortex shedding instability is likely damped by the severe confinement effect of the channel walls (59). The case with $d/W=0.50$, for

which $Re_d=100$, does generate vortex shedding and provides data for comparison with the flutter mixer. Fortunately, this diameter is also quite comparable to the amplitude of the fluttering membrane with $L=W/2$ at this Reynolds number and this further facilitates the comparison between the two cases.

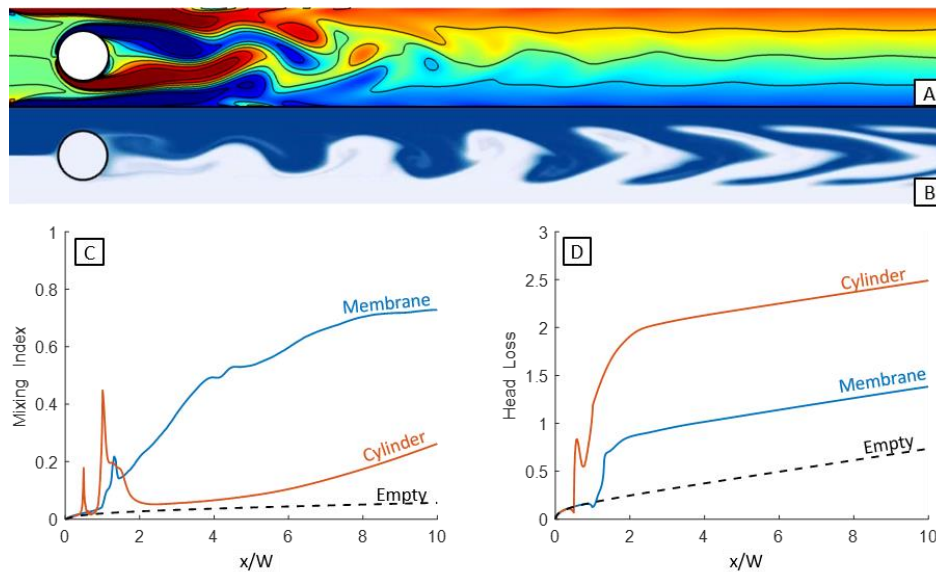


FIG. 10 – Comparison of a cylinder and the $L=W/2$ membrane case with snapshots of (A) the spanwise vorticity ω , (B) the scalar field ϕ , as well as plots of the (C) the Avg Mixing Index and (D) the head loss for the $R=100$, $Sc=100$ cases.

FIG. 10 shows the contour plots depicting the vortex shedding and scalar mixing for this mixer and these can be directly compared to the corresponding plots in FIG. 3. It is clear that although both cases exhibit vortex shedding, the vortex topology and scalar transport are quite different. In particular, while the membrane sheds vortices near the outer walls of channel and forms an inverse vortex street (counterclockwise vortices on top and clockwise vortices on the bottom) where the shed vortices convect along the outer walls, the cylinder generates a conventional Karman vortex street with the vortices convecting near the centerline of the channel. A consequence of this difference in the vortex topology is that the wake vortices of the element are more effective in inducing a downward advection of the scalar from the wall into the core of the fluid. In contrast, the cylinder wake vortices primarily perturb the scalar field near the channel centerline and only have a marginal effect on the scalar concentration in the vicinity of the channel walls.

From a quantitative perspective (FIG. 10), the flutter mixer outperforms the post mixer both in terms of mixing and head loss by a significant margin. The flutter mixer shows a rapid increase in mixing between $x/W=2$ and 4 whereas, the cylinder mixer has a very slow increase in mixing index in this region (note that for this plot, we ignore the region with the cylinder where the mixing index is not meaningful). Consequently, the mixing index for the cylinder at $x/W=10$ is only 0.26, which is about 2.8 times smaller than that for the flutter mixer. Furthermore, while the additional head loss for the flutter mixer at the outlet was 0.65, the additional head loss for the cylinder is 1.76, which is 2.7 times higher than the flutter mixer. This is in line with the fact that bluff-bodies are associated with a significant drag, whereas the fluttering element is fairly streamlined and is associated with an overall lower magnitude of total drag. This difference in performance is clearly seen in the scatter plot seen in FIG. 7, wherein the post mixer at $Re=200$ shows better mixing than the empty channel, but underperforms significantly compared to the

flutter mixer and also generates significant pressure loss. Thus, in summary, flow-induced flutter is a significantly more effective mixing mechanism than bluff-body vortex shedding.

Summary

Computational modeling has been used to explore the fluid dynamics and mixing performance of an inertial-scale micromixer where mixing is enhanced by the flow-induced flutter of an elastic membrane. Simulations show that significant flutter and flutter-induced enhancement of mixing is achievable at channel Reynolds number as low as 15 and the mixing performance improves with Reynolds number. The enhanced mixing is associated with the shedding of vortices from the trailing-edge of the fluttering membrane and the organization of these vortices into an inverse Karman vortex street that generates significant cross-stream advection of the scalar and highly complex interfaces across which diffusive mixing can occur. The mixing mechanism in these flutter mixers is found to be effective over a large range of mass diffusivities. Comparison of the flutter mixer with a “post” micromixer that employs bluff-body induced vortex shedding for mixing shows that the flutter mixer generates significantly higher mixing with much lower pressure loss.

The current work also has limitations. First, the geometric model of the mixer is very simple (a straight channel) and two-dimensional. Actual micromixers have duct-like channels where three-dimensional flow effects are significant. Furthermore, three-dimensionality could potentially affect the flutter of the elastic element and the flow field. While previous investigations have shown that the flutter-instability of such membranes is robust to three-dimensional effects (25, 58, 60, 61), it is worthwhile to explore this using 3D computational models. This is currently being done and results will be reported in the future.

Appendix – Grid Convergence

The flow solver in ViCar3D has been extensively validated (47, 49). Furthermore, the FSI model used in this study has been benchmarked in multiple papers (24, 50, 51). However, additional tests have been conducted for the $Re = 200$, $Sc = 100$ and $L=W/2$ case to demonstrate grid convergence for the current problem. First, the default resolution was chosen according to prior work such that $dx = dy = 0.016$, $ds = 0.012$, and $dt = 0.0001$ (1280x128 fluid points and 80 points on the membrane). Then the fluid resolution in each direction and the structure resolution was increased by a factor of 1.5, leading to a total of 2.25 times more fluid points (1920x192 fluid points). Concurrently, the temporal resolution was doubled to $dt = 5 \times 10^{-5}$. The mixing index and head loss were computed and compared between the two grids; the head loss saw almost no change (<0.1%) and this was expected as the baseline resolution was based in our previous studies of a similar configuration(24). The mixing index also changed by at most 3% in the channel at the higher resolution, indicating that the simulations on the baseline grid are also quite adequately converged.

Acknowledgements

The development of the flow solver has benefited from support from AFOSR Grant FA9550-16-1-0404 and NSF IIS Grant 1344772. Discussions with Dr. Kourosh Shoele on the technical aspects of the fluid-structure interaction modeling are acknowledged. Comments from Dr. Claire Hur on a draft of the manuscript are also acknowledged.

References

1. Amini H, Lee W, Di Carlo D. Inertial microfluidic physics. *Lab Chip*. 2014 Aug 07;;14(15):2739-61.
2. Stone HA, Stroock AD, Ajdari A. Engineering flows in small devices: microfluidics toward a lab-on-a-chip. *Annu.Rev.Fluid Mech*. 2004;36:381-411.
3. Nguyen N, Wu Z. Micromixers—a review. *J Micromech Microengineering*. 2004;15(2):R1.
4. Capretto L, Cheng W, Hill M, Zhang X. Micromixing within microfluidic devices. *Microfluidics*. 2011. p. 27-68.
5. Lee C, Chang C, Wang Y, Fu L. Microfluidic mixing: a review. *International journal of molecular sciences*. 2011;12(5):3263-87.
6. Lee C, Wang W, Liu C, Fu L. Passive mixers in microfluidic systems: A review. *Chemical Engineering Journal*. 2016;288:146-60.
7. Zhang J, Yan S, Yuan D, Alici G, Nguyen N, Warkiani ME, et al. Fundamentals and applications of inertial microfluidics: a review. *Lab on a Chip*. 2016;16(1):10-34.
8. Cai G, Xue L, Zhang H, Lin J. A review on micromixers. *Micromachines*. 2017;8(9):274.
9. Glasgow I, Aubry N. Enhancement of microfluidic mixing using time pulsing. *Lab on a Chip*. 2003;3(2):114-20.
10. Xia Q, Zhong S. Liquid mixing enhanced by pulse width modulation in a Y-shaped jet configuration. *Fluid Dyn Res*. 2013;45(2):025504.
11. Afzal A, Kim K. Convergent–divergent micromixer coupled with pulsatile flow. *Sensors and Actuators B: Chemical*. 2015;211:198-205.
12. Ryu KS, Shaikh K, Goluch E, Fan Z, Liu C. Micro magnetic stir-bar mixer integrated with parylene microfluidic channels. *Lab on a Chip*. 2004;4(6):608-13.
13. Khatavkar VV, Anderson PD, den Toonder JM, Meijer HE. Active micromixer based on artificial cilia. *Phys Fluids*. 2007;19(8):083605.
14. Oddy MH, Santiago JG, Mikkelsen JC. Electrokinetic instability micromixing. *Anal Chem*. 2001;73(24):5822-32.
15. Tai C, Yang R, Huang M, Liu C, Tsai C, Fu L. Micromixer utilizing electrokinetic instability-induced shedding effect. *Electrophoresis*. 2006;27(24):4982-90.
16. Ahmed D, Mao X, Shi J, Juluri BK, Huang TJ. A millisecond micromixer via single-bubble-based acoustic streaming. *Lab on a chip*. 2009 Sep 21;;9(18):2738.

Physical Review Fluids, 4(5), p.054501

<https://doi.org/10.1103/PhysRevFluids.4.054501>

17. Van Phan H, Coşkun MB, Şeşen M, Pandraud G, Neild A, Alan T. Vibrating membrane with discontinuities for rapid and efficient microfluidic mixing. *Lab on a Chip*. 2015;15(21):4206-16.
18. Cui W, Zhang H, Zhang H, Yang Y, He M, Qu H, et al. Localized ultrahigh frequency acoustic fields induced micro-vortices for submillisecond microfluidic mixing. *Appl Phys Lett*. 2016;109(25):253503.
19. Hossain S, Ansari MA, Kim K. Evaluation of the mixing performance of three passive micromixers. *Chem Eng J*. 2009;150(2-3):492-501.
20. Afzal A, Kim K. Passive split and recombination micromixer with convergent–divergent walls. *Chemical Engineering Journal*. 2012;203:182-92.
21. Stroock AD, Dertinger SK, Ajdari A, Mezić I, Stone HA, Whitesides GM. Chaotic mixer for microchannels. *Science*. 2002;295(5555):647-51.
22. Wu Z, Nguyen N. Convective–diffusive transport in parallel lamination micromixers. *Microfluidics and Nanofluidics*. 2005;1(3):208-17.
23. Herrault F, Hidalgo PA, Ji C-, Glezer A, Allen MG. Cooling performance of micromachined self-oscillating reed actuators in heat transfer channels with integrated diagnostics. 2012 IEEE 25th International Conference on Micro Electro Mechanical Systems (MEMS); January 2012.
24. Shoele K, Mittal R. Computational study of flow-induced vibration of a reed in a channel and effect on convective heat transfer. *Physics of Fluids*. 2014 Dec;26(12):127103.
25. Rips A, Shoele K, Glezer A, Mittal R. Efficient electronic cooling via flow-induced vibrations. *Thermal Measurement, Modeling & Management Symposium (SEMI-THERM)*, 2017 33rd; IEEE; 2017.
26. Zhang J, Childress S, Libchaber A, Shelley M. Flexible filaments in a flowing soap film as a model for one-dimensional flags in a two-dimensional wind. *Nature*. 2000 Dec 14;408(6814):835-9.
27. Shelley MJ, Zhang J. Flapping and Bending Bodies Interacting with Fluid Flows. *Annual Review of Fluid Mechanics*. 2011 Jan 21;43(1):449-65.
28. Kim D, Cossé J, Huertas Cerdeira C, Gharib M. Flapping dynamics of an inverted flag. *Journal of Fluid Mechanics*. 2013 Dec;736.
29. Taneda S. Waving Motions of Flags. *J Phys Soc Jpn*. 1968;24(2):392-401.
30. Eloy C, Lagrange R, Souilliez C, Schouveiler L. Aeroelastic instability of cantilevered flexible plates in uniform flow. *J Fluid Mech*. 2008;611:97-106.
31. Ait Abderrahmane H, Païdoussis MP, Fayed M, Dick Ng H. Nonlinear dynamics of silk and Mylar flags flapping in axial flow. *Journal of Wind Engineering and Industrial Aerodynamics*. 2012;107-108:225-36.
32. Dessi D, Mazzocconi S. Aeroelastic behavior of a flag in ground effect. *Journal of Fluids and Structures*. 2015;55:303-23.

Physical Review Fluids, 4(5), p.054501

<https://doi.org/10.1103/PhysRevFluids.4.054501>

33. Gibbs SC, Sethna A, Wang I, Tang D, Dowell E. Aeroelastic stability of a cantilevered plate in yawed subsonic flow. *Journal of Fluids and Structures*. 2014; 49:450-62.
34. Alben S. The flapping-flag instability as a nonlinear eigenvalue problem. *Phys Fluids*. 2008; 20(10):104106.
35. Alben S. Optimal flexibility of a flapping appendage in an inviscid fluid. *J Fluid Mech*. 2008;14:355-80.
36. Alben S. Flag flutter in inviscid channel flow. *Phys Fluids*. 2015;27(3):033603.
37. Alben S, Shelley MJ. Flapping States of a Flag in an Inviscid Fluid: Bistability and the Transition to Chaos. *Phys Rev Lett*. 2008;100(7):074301.
38. Argentina M, Mahadevan L. Fluid-flow-induced flutter of a flag. *Proc Natl Acad Sci U S A*. 2005;102(6):1829.
39. Kornecki A, Dowell EH, O'Brien J. On the aeroelastic instability of two-dimensional panels in uniform incompressible flow. *Journal of Sound and Vibration*. 1976;47(2):163-78.
40. Eloy C, Souilliez C, Schouveiler L. Flutter of a rectangular plate. *Journal of Fluids and Structures*. 2007;23(6):904-19.
41. Doaré O, Sauzade M, Eloy C. Flutter of an elastic plate in a channel flow: Confinement and finite-size effects. *Journal of Fluids and Structures*. 2011 January 1;;27(1):76-88.
42. Theodorsen T. *General Theory of Aerodynamic Instability and the Mechanism of Flutter*. Langley, VA: US National Advisory Committee for Aeronautics; 1935.
43. Huang W, Shin SJ, Sung HJ. Simulation of flexible filaments in a uniform flow by the immersed boundary method. *Journal of Computational Physics*. 2007 Oct 1;;226(2):2206-28.
44. Zhu L, Peskin CS. Simulation of a flapping flexible filament in a flowing soap film by the immersed boundary method. *Journal of Computational Physics*. 2002;179(2):452-68.
45. Connell BSH, Yue DKP. Flapping dynamics of a flag in a uniform stream. *J Fluid Mech*. 2007;581:33-67.
46. Trethewey DC, Meinhart CD. Apparent fluid slip at hydrophobic microchannel walls. *Phys Fluids*. 2002;14(3):L12.
47. Mittal R, Dong H, Bozkurttas M, Najjar FM, Vargas A, von Loebbecke A. A versatile sharp interface immersed boundary method for incompressible flows with complex boundaries. *Journal of computational physics*. 2008;227(10):4825-52.
48. Zhu C, Seo JH, Vedula V, Mittal R. A Highly Scalable Sharp-Interface Immersed Boundary Method for Large-Scale Parallel Computers. 23rd AIAA Computational Fluid Dynamics Conference; ; 2017.

Physical Review Fluids, 4(5), p.054501

<https://doi.org/10.1103/PhysRevFluids.4.054501>

49. Seo JH, Mittal R. A sharp-interface immersed boundary method with improved mass conservation and reduced spurious pressure oscillations. *Journal of computational physics*. 2011;230(19):7347-63.
50. Shoele K, Zhu Q. Leading edge strengthening and the propulsion performance of flexible ray fins. *J Fluid Mech*. 2012;693:402-32.
51. Shoele K, Mittal R. Energy harvesting by flow-induced flutter in a simple model of an inverted piezoelectric flag. *J Fluid Mech*. 2016;790:582-606.
52. Goldstein D, Handler R, Sirovich L. Modeling a no-slip flow boundary with an external force field. *Journal of Computational Physics*. 1993;105(2):354-66.
53. Danckwerts PV. The definition and measurement of some characteristics of mixtures. *Applied Scientific Research, Section A*. 1952;3(4):279-96.
54. Liscinsky D, True B, Holdeman J. Experimental investigation of crossflow jet mixing in a rectangular duct. 29th Joint Propulsion Conference and Exhibit; ; 1993.
55. Kockmann N, Kiefer T, Engler M, Woias P. Convective mixing and chemical reactions in microchannels with high flow rates. *Sensors Actuators B: Chem*. 2006;117(2):495-508.
56. Dong H, Mittal R, Najjar FM. Wake topology and hydrodynamic performance of low-aspect-ratio flapping foils. *J Fluid Mech*. 2006;566:309-43.
57. Deshmukh SR, Vlachos DG. Novel micromixers driven by flow instabilities: Application to post-reactors. *AIChE J*. 2005;51(12):3193-204.
58. Shoele K, Mittal R. Flutter instability of a thin flexible plate in a channel. *J Fluid Mech*. 2016;786:29-46.
59. Sahin M, Owens RG. A numerical investigation of wall effects up to high blockage ratios on two-dimensional flow past a confined circular cylinder. *Phys Fluids*. 2004;16(5):1305-20.
60. Huang W, Sung HJ. Three-dimensional simulation of a flapping flag in a uniform flow. *J Fluid Mech*. 2010;653:301-36.
61. Dong D, Chen W, Shi S. Coupling motion and energy harvesting of two side-by-side flexible plates in a 3D uniform flow. *Applied Sciences*. 2016;6(5):141.